

An analysis of recorded and simulated SH wave reverberations in the upper mantle beneath the USArray

Meichen Liu^{1,#}, Jeroen Ritsema¹, and Carlos Chaves²

¹ Department of Earth and Environmental Sciences, University of Michigan, 1100 North University Avenue, Ann Arbor, MI 48109, USA.

² Departamento de Geofísica, Instituto de Astronomia, Geofísica e Ciências Atmosféricas, Universidade de São Paulo, Rua do Matão 1226, São Paulo, São Paulo, Brasil.

Corresponding author: Meichen Liu (meichenl@umich.edu)

Summary

Long-period ($T > 10$ s) shear-wave reverberations between the surface and reflecting boundaries below seismic stations are useful for studying the mantle transition zone (MTZ) but finite-frequency effects may complicate the interpretation of waveform stacks. Using waveform data from the USArray and spectral-element method synthetics for 3-D seismic models, we illustrate that a common-reflection point (CRP) modeling of layering in the upper mantle must be based on 3-D reference structures and accurate calculations of reverberation traveltimes. Our CRP mapping of recorded waveforms places the 410-km and 660-km phase boundaries about 15 km deeper beneath the western US than beneath the central-eastern US if it is based on the 1-D PREM model. The apparent east-to-west deepening of the MTZ disappears in the CRP image if we account for shear-wave velocity variations in the mantle. We also find that ray theory overpredicts the traveltime delays of the reverberations if 3-D velocity variations in the mantle are prescribed by global models S40RTS, SEMUCB-WM1, and TX2015. Undulations of the 410-km and 660-km are underestimated in the analysis when their wavelengths are smaller than the Fresnel zones of the wave reverberations in the MTZ.

Keywords: North America; Time-series analysis; Body waves; Seismic tomography.

1. Introduction

Recordings of long-period ($T > 10$ s) shear waves are useful data to map seismic discontinuities and velocity gradients in the mantle transition zone (MTZ) (e.g., [Shearer, 1990](#)). The mineral-phase transitions near depths of 410 and 660 km produce the highest amplitude shear-wave reflections after the S wave arrival (e.g., [Shearer and Buehler, 2019](#)), before the SS arrival (e.g., [Flanagan and Shearer, 1998](#)), and between multiple ScS reflections (e.g., [Revenaugh and Jordan, 1991](#)) in stacks of transverse-component seismograms. We call these boundaries the “410” and “660” in this paper and define the MTZ as the layer of the mantle between the 410 and 660. Constraints on the depths of the 410 and 660 and the thickness of the MTZ constrain the temperature and composition of the mantle (e.g., [Bina and Hellfrich, 1994](#); [Xu et al. 2009](#)) and heat and mass transfer between the upper and lower mantle.

Most seismological studies of hundreds to thousands of waveforms are based on 1-D seismic reference profiles and ray theory to facilitate the analysis and computations. However, long-period shear waves are sensitive to seismic structure in the mantle beyond the geometric ray so ray-theoretical calculations of traveltimes and waveform shifts may be inaccurate (e.g., [Tromp et al., 2005](#)). Modeling inaccuracies have been discussed thoroughly for the SS wave and its precursors (e.g., [Neele et al., 1997](#); [Zhao and Chevrot, 2003](#); [Bai et al., 2012](#); [Guo and Zhou, 2020](#); [Koroni and Trampert, 2016, 2021](#)), but they apply to all long-period seismic wave reflections and conversions in the MTZ, including the multiple ScS reverberations (e.g., [Haugland et al., 2020](#)) and receiver functions (e.g., [Deng and Zhou, 2015](#)).

The receiver-side shear-wave reverberation in the upper mantle is the phase of interest in this paper. It has been introduced by [Shearer and Buehler \(2019\)](#), a study we abbreviate as SB19 from hereon, as a new wave type for probing the upper mantle and the MTZ. Using USArray waveforms and a common-reflection-point (CRP) imaging method, SB19 estimated the depths of the 410 and 660 to be 40–50 km deeper beneath the western US than beneath the central and eastern US. This is an important study outcome as it implies that the seismic contrast in the uppermost mantle beneath the tectonically active western US and tectonically stable central and eastern US extends into the MTZ.

SB19 used ray theory and the 1-D iasp91 velocity model to relate traveltimes to reflector depth. They acknowledged that 3-D seismic velocity heterogeneity may have a significant effect on the amplitude, coherence, and depths of the 410 and the 660 in the CRP images. In this paper, we follow up on their recommendation to investigate how 3-D velocity structure changes the interpretation of CRP imaging results and to test the hypothesis that the 410 and 660 beneath the US are unperturbed. Using a stacking method instead of an inversion method we confirm that reverberation traveltimes are longer and therefore that the 410 and 660 are 40–50 km deeper beneath the western US than the central-eastern US if the analysis is based on a 1-D reference structure (section 2). We explore how strongly 3-D shear-velocity heterogeneity, as constrained by global tomography, perturb reverberation traveltimes and how ray-theoretical traveltime corrections change the CRP images (section 3). Using spectral-element method seismograms we evaluate the accuracy of ray theory in predicting the reverberation traveltimes and whether undulations on the 410 and 660 are resolvable by long-period shear wave reflections (section 4). In section 5, we discuss our key findings.

2. Mapping of the 410 and 660 by 1-D common reflection point imaging

2.1 The Ssds phase

A shear-wave reverberation beneath the receiver is abbreviated here as “Ssds” following the notation of SB19. Ssds is a shear-wave that follows a similar path in the mantle as the direct S wave and reflects off the free surface and off the top of a reflector at depth d before it is recorded by a seismometer on the surface (Figure 1). The arrival time of Ssds after S depends primarily on the reflector depth d and the shear-wave speed above the reflecting layer. For PREM, an earthquake at the surface, and an epicentral distance of 80° , Ss410s and Ss660s arrive 159.6 s and 242.2 s after S, respectively. Ssds can interfere with SS precursors but the two phases have different slownesses and are distinguishable in waveforms recorded over a wide epicentral distance range. The top-side reflection sdsS near the source has the same traveltime as Ssds at any distance for a 1-D velocity structure. For stations at similar azimuths, source-side reflection points are virtually identical whereas the Ssds reflection points are separated beneath the arrays of stations. Therefore, variations in the Ssds traveltime are primarily due to seismic structure in the upper mantle beneath the seismic stations. There is no source-side and receiver side ambiguity if the analysis is limited to earthquakes deeper than the reflecting boundaries of interest (Liu and Shearer, 2021) but the data set would be significantly smaller.

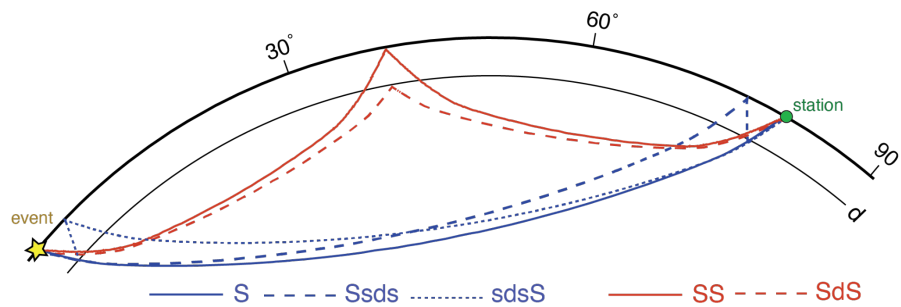
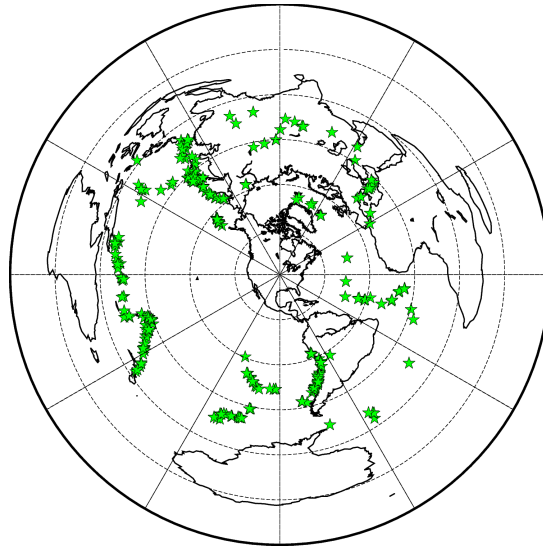


Figure 1. Ray diagram of the phases S (solid blue line), Ssds (dashed blue line), sdsS (dotted blue line), SS (solid red line) and the SS precursor SdS (dashed red line) for an epicentral distance of 80 degrees.

2.2 USArray waveforms

Our data set includes 59,517 transverse-component displacement waveforms from 337 global earthquakes (Figure 2) recorded by stations from the USArray and other regional networks in the forty-eight conterminous United States. The earthquakes are shallower than 35 km, so the direct and depth phases form a single pulse at long periods. The earthquakes have moment magnitudes smaller than 7.0 so rupture complexity does not affect the long-period waveforms strongly. The epicentral distances are between 60° and 110° and waveforms have been filtered using a bandpass Butterworth filter with corner frequencies of 20 mHz and 80 mHz. We align the waveforms on the peak S-wave displacement and normalize them, so the S waves have the same polarities and maximum displacements of +1. In all waveforms, the S-wave displacement is at least six times larger than the signal in the 100-s long window prior to the S wave onset. The maximum and the root-mean-square displacement in the window [30 s, 220 s] after the S-wave arrival time are six times and three times smaller than the peak S-wave displacement, respectively. We remove earthquakes with fewer than 20 seismograms left after these quality control steps.

112



113

114

115

116

Figure 2. (stars) Epicenters of earthquakes used in this study. The dashed circles have a common center of [40N, -95E] and radii of 30, 60, 90, 120, and 150 degrees.

117

118

119

120

121

122

123

124

125

126

127

128

A record section of the sum of these waveforms bring out Ss410s and Ss660s as the strongest mantle reflections (Figure 3). The Ss410s and Ss660s have mean amplitudes of about 0.05 and are recorded without interference with ScS and SS at distances larger than 60° and 75°, respectively. The SS precursors S410S and S660S are weaker than Ss410s and Ss660s at distances smaller than 110° (e.g., Shearer, 1991). The signal labeled ‘A’ in Figure 3a, which arrives about 50 seconds before SS, appears to be an SS-precursor reflection at a depth of about 125 km. The signals near the label ‘B’ in Figure 3a between about 45 and 70 seconds may be Ssds reflections from the lithosphere-asthenosphere boundary (LAB), a boundary that has also been studied with P-wave and S-wave receiver functions (Rychert et al., 2007; Abt et al., 2010; Hopper and Fischer, 2018) and multiple S-wave reflection (Liu and Shearer, 2021). We suspect that the signal 45 s after S with a positive polarity is a side lobe due to the applied butterworth filter because a signal with similar strength is present about 45 s before S.

129

130

131

132

133

134

135

136

137

138

Ssds reflections from the uppermost lower mantle below the 660 arrive more than 250 s after S and do not interfere with SS and the S410S precursor at distances larger than 95° in region ‘C’ of Figure 3a. However, it is difficult to differentiate reflections below the 660 from shallower SS precursors because S waves are attenuated by diffraction around the core and slowness resolution is poor. The high-amplitude signal about 330 s after S has a slowness of roughly 1.0 sec/degree which is smaller than the slowness of any SS precursor. Its traveltimes is similar to that of the phases Ss410s410s (i.e., the shear-wave reverberation with two up-and-down shear-wave segments between the surface and the 410) and the phase PSs660s (i.e the PS phase with an additional top-side reflection off the 660). However, it is unlikely that these phases can be recorded with high amplitudes on transverse component records.

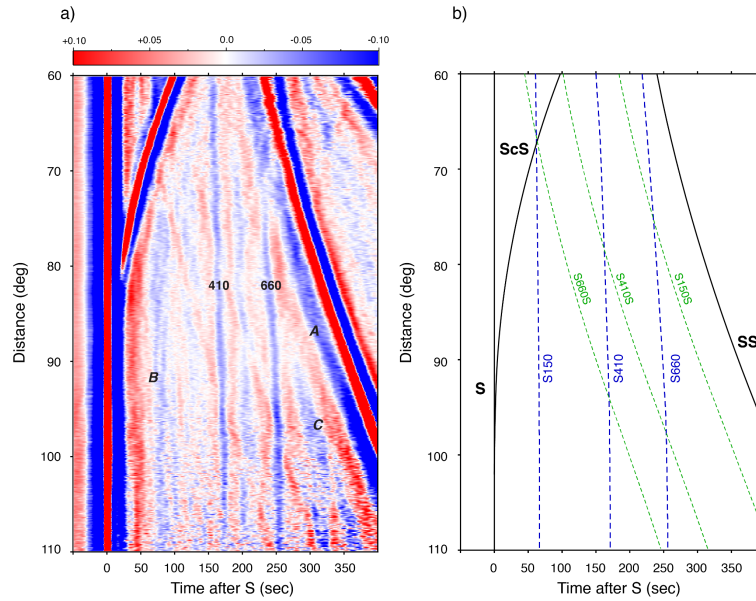


Figure 3. (a) Record section of transverse component seismograms used in this study. Shown is the amplitude of ground displacement in red and blue for positive and negative polarities, respectively, with a color intensity proportional to the absolute value. The seismograms have been aligned to the S wave at time 0. (b) The arrival times of S, ScS, and SS (black lines), S150, S410 and S660 (blue dashed lines), and the SS-precursors S150S, S410S and S660S (green dashed lines) have been computed for PREM for a source depth of 20 km.

2.3 Common reflection point imaging

By 1-D common reflection point (CRP) mapping we convert the Ssds-S difference times to the locations of the Ssds reflecting points in the upper 800 km of the mantle beneath the USArray. We use the TauP software (Crotwell et al., 1999) and the PREM velocity structure to calculate Ssds reflection points and traveltimes. At a depth d , 1,716 reflection points are uniformly distributed on a $1^\circ \times 1^\circ$ horizontal grid between 25°N and 50°N and between -130°E and -65°E . The horizontal grids are separated by 5 km from 10 to 1,000 km, for a total of 199 depths. For a gridpoint X , we select waveforms for which the Ssds reflection points are within the $1^\circ \times 1^\circ$ bin around X and for which the theoretical Ssds arrival time differs more than 15 s from the theoretical arrival times of sS, ScS, and sScS, and more than 50 s from the arrival time of SS to avoid wave interference. If fewer than five waveforms are available, we deem the mean displacement of Ssds to be inaccurately determined.

Since we use shallow focus earthquakes, the source-side and the receiver-side reflections have identical traveltimes. From synthetic seismograms for PREM, we have verified that they are equally strong so we attribute half of the mean Ssds amplitude to a source-side reflection. To construct the CRP images, we estimate source-side and receiver-side reflections sequentially for each of the 337 earthquakes following three steps. First, we determine the mean of the Ssds displacement at the theoretical arrival time of Ssds for all seismograms. Second, we subtract this mean value from the Ssds displacement of each waveform. Third, we assume the residual displacement to be due to reflections beneath the USArray. After mapping the Ssds signals onto the grid ray theoretically, we average the receiver-side reflection amplitudes within $1^\circ \times 1^\circ$ bins, which are narrower than the Fresnel zones of 10-s period Ssds reflections in the mantle transition zone, as shown by SB19. We have also implemented the approach by SB19, who estimate the source-side

and receiver-side contributions to Ssds in one step using a sparse-matrix inversion solver. This approach yields smaller amplitudes of the Ssds reflections but the overall character of the CRP image, including the depths of the 410 and 660, are similar (Supplementary Figure 1).

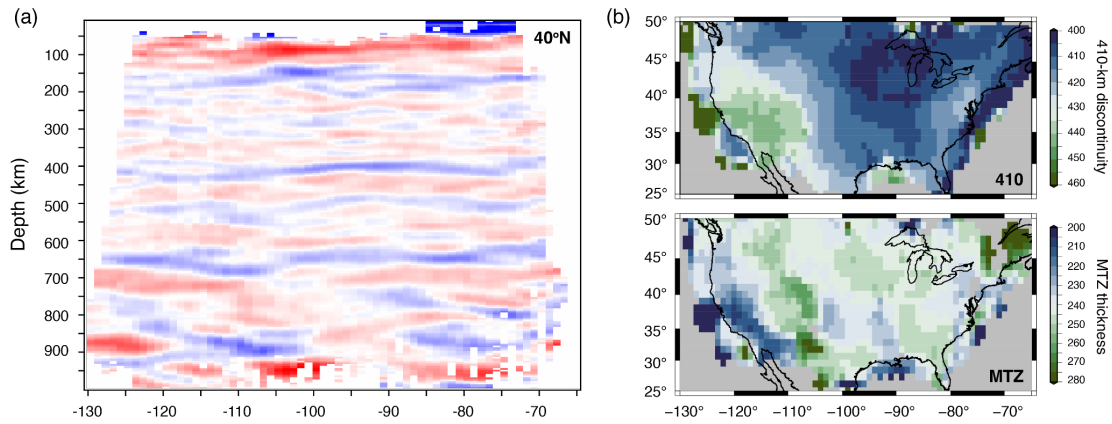


Figure 4. (a) Vertical section of the CRP image along 40°N. Red and blue indicate positive and negative polarities, respectively. The color scale used is the same as in Figure 3. (b) Depth of the 410 (top) and the thickness of the mantle transition zone (bottom).

Figure 4a shows a vertical section of the CRP image along the 40°N parallel. As expected from Figure 3, the 410 and 660 are the clearest reflectors. Variations of the Ss410s-S and Ss660s-S difference times project as spatial variations in the depth of 410 and 660. The 410 and 660 are deeper and more complex beneath the western US (west of -100°E) than beneath the central and eastern US. This is also apparent in other sections through the CRP images, not shown here. The 410 is strongest between longitudes -100°E and -75°E. The 520-km discontinuity may be responsible for a relatively weak Ssds reflection between the 410 and 660. The CRP images near the 410 and 660 west of -100°E are complex, which was also noted by SB19. Strong reflectors corresponding to the Ssds signals in region B of the record section of Figure 3 are mapped at about 100 km and 150 km depth, but their depths and strengths vary. The incoherent structures at depths larger than 800 km are most likely imaging artifacts because these structures correspond to the amplified signals in region C of Figure 3, where S are diffracting waves and slowness resolution is relatively poor.

Figure 4b shows maps of the depth of the 410 and the thickness of the MTZ. These are estimated from the absolute minimum values of the mean displacements in the CRP image in the depth ranges of 350–470 km (for the 410) and 620–730 km (for the 660) by cubic spline interpolation. We do not estimate the depth of the 410 and 660 where a secondary absolute minimum is stronger than 40% of the absolute minimum in these depth ranges. The depth of the 410 varies by 40–50 km. The 410 is deepest beneath the southern Basin and Range and the Colorado Plateau and shallowest beneath the central plains and the Atlantic coast. The thickness of the MTZ varies less than 10 km because the 410 and 660 depth variations are similar. The MTZ is thinnest beneath California and thickest beneath the Southern Rocky Mountains and the Colorado plateau. The MTZ thickness is anomalous in small regions near the margins of our model domain. This includes the extremely thin (210 km) MTZ beneath the west coast of central California which was also resolved by SB19. However, the CRP images have low resolution here because the data coverage is poor.

SB19 resolved similar maps as Figure 4b, indicating that our and SB19's data sets contain consistent variations of the Ss410s-S and Ss660s-S difference times and that estimates of the depths of the 410 and 660 do not strongly depend on the applied mapping method.

3. Influence of 3-D seismic heterogeneity on the CRP images

The map of the depth of the 410 shown in Figure 4b is reminiscent of the estimated shear-wave velocity variations in the upper mantle beneath the US from the modeling of regional S-waves (e.g., Grand and Helmberger, 1984), surface-waves (e.g., Van der Lee and Nolet, 1997), and, more recently, ambient noise (e.g., Bensen et al., 2008), P-wave polarization (Park et al., 2019) and surface-wave amplification (Eddy & Ekstrom, 2014; Bowden & Tsai, 2017). This indicates strongly that shear-velocity variations in the mantle affect Ss410s-S and Ss660s-S difference times and that a mapping method based on a 1-D velocity structure would overestimate undulations of the 410 and 660.

3.1 S-wave traveltimes variations

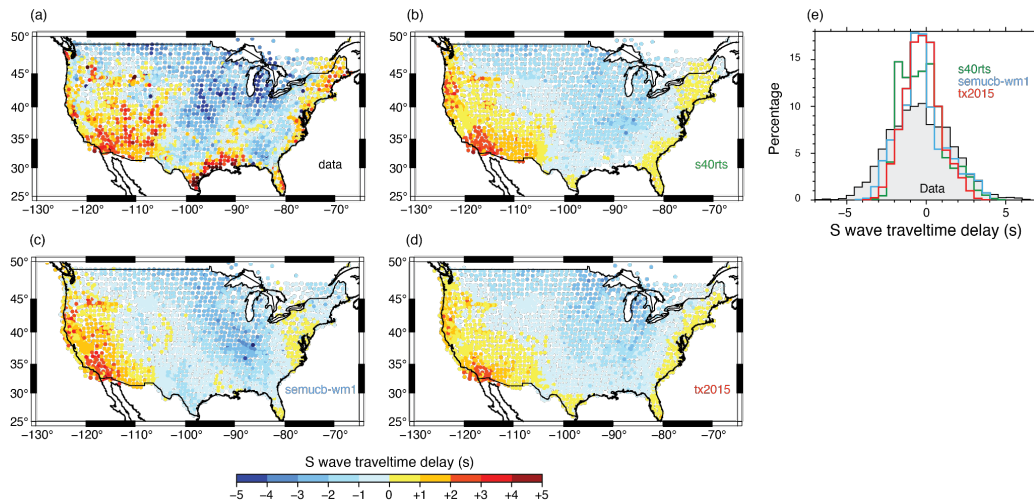


Figure 5. The recorded (a) and predicted (b, c, d) traveltimes delays of S waves by tomographic models S40RTS (in b), SEMUCB-WM1 (in c), and TX2015 (in d). Each circle indicates the location of a seismic station. Its color indicates the mean of the S-wave traveltimes delays with respect to the PREM model for at least five S waves. (e) Histograms of the S wave traveltimes delay in the data (grey fill) and predictions by S40RTS (green line), SEMUCB-WM1 (blue line), and TX2015 (red line) for the stations in panels a–d.

Figure 5a shows shear-wave velocity variations in the upper mantle affect the traveltimes of S waves. Plotted are the average S-wave delay with respect to the PREM velocity model of at least five S-waves recorded at seismic stations from the USArray. The delay times have been corrected for ‘source terms’, representing the effects of a potential mislocation of the earthquake location and origin time on the absolute S wave traveltimes. S waves recorded by USArray stations in the western US (the tectonically active region) arrive on average 5–6 seconds later than at stations in the central and eastern US (the stable platform). The global-scale mantle models S40RTS (Ritsema et al., 2011), SEMUCB-WM1 (French & Romanowicz, 2014), and TX2015 (Lu & Grand, 2016) predict a similar traveltimes pattern (Figures 5b–d) but the range is slightly smaller than in the data (Figures 5e). Our calculations, not included in Figure 5, indicate that the

crustal structure from CRUST1.0 (Laske et al., 2013) enhances the east-west contrast only slightly, so wave speed variations in the mantle are primarily responsible for the S-wave traveltime differences.

The imperfect match between the recorded and the predicted S wave traveltime is expected because tomographic models do not perfectly explain the recorded traveltime variation of any shear-wave (e.g., Ritsema et al., 2004). Nevertheless, it is obvious that shear-velocity heterogeneity affects teleseismic S wave traveltimes across the USArray. Since Ssds has two additional propagation legs through the upper mantle, the Ss410s-S and Ss660s-S difference times are likely to be double the variation shown in Figure 5a due to shear velocity heterogeneity only. If shear wave speed variations in the upper mantle beneath North America are ignored in the modeling, a variation of the Ss410s-S and Ss660s-S difference times of more than 10 s would imply that the depths of the 410 and 660 vary by about 18 and 20 km or more. This is of the same magnitude as resolved in Figure 4.

3.2 Ray-theoretical corrections

Since the tomographically predicted S-wave traveltime variation of 5–6 seconds across the USArray is a significant fraction of the recorded traveltime variation, we suspect that shear-velocity variations in the upper mantle influence the CRP imaging and our estimate of the 410 depth. To quantify this, we determine the CRP image for “corrected” Ssds-S difference times. From the measured Ssds-S difference time, we subtract the predicted difference time anomaly (positive or negative) by shifting a 5-s wide segment of the waveform around the theoretical Ssds arrival time. We predict the Ssds-S difference time by ray tracing through S40RTS, SEMUCB-WM1, or TX2015. In the calculations, we do not include a crust in the velocity models so Ssds-S difference times are artificially short by about 3.5 s.

Figure 6a shows the CRP image along the 40°N parallel after travel time corrections using S40RTS. The images for SEMUCB-WM1 and TX2015 are similar, as expected from Figure 5. Compared to the uncorrected profile shown in Figure 4a, The character of the corrected and uncorrected CRP images are the same but the 410 and 660 are flatter boundaries across the USArray. This is especially clear for the region between -100°E and -80°E where the 410 and 660 are relatively simple. Figure 6b emphasizes that the depth variations of the 410 is smaller when the CRP image is based on tomographically corrected Ssds-S difference times. The thickness of the MTZ in the corrected and uncorrected images are similar because shear velocity variations are relatively weak in the MTZ compared to the uppermost mantle. The histograms shown in Figures 6c illustrate that the depth variation of the 410 is about a factor of two smaller when traveltime corrections have been applied to the data and that the corrections do not change the range in MTZ thickness values. The travel time corrections change the mean depth of the 410 and 660 by about 10 km, which is similar to the change obtained by Shearer & Buehler (2019) using ray-theoretical corrections computed for a regional 3-D velocity model. The 410 and 660 are imaged deeper than for the uncorrected waveforms because we underpredict Ssds-S traveltimes in our calculation by excluding the crust in the velocity model.

One cannot argue that the ray-theoretically corrected images reflect the actual depth variations of the 410. Since S40RTS and any other tomographic model does not explain perfectly the recorded S-wave traveltime variation (see Figure 3), it is unlikely that the traveltimes corrections have not completely removed the effects of the shear-velocity structure on the CRP image. Further, we show in the next section that ray-

theoretical predictions of long-period Ssds-S traveltimes are inaccurate and that corrections can project as spurious signals in the CRP images.

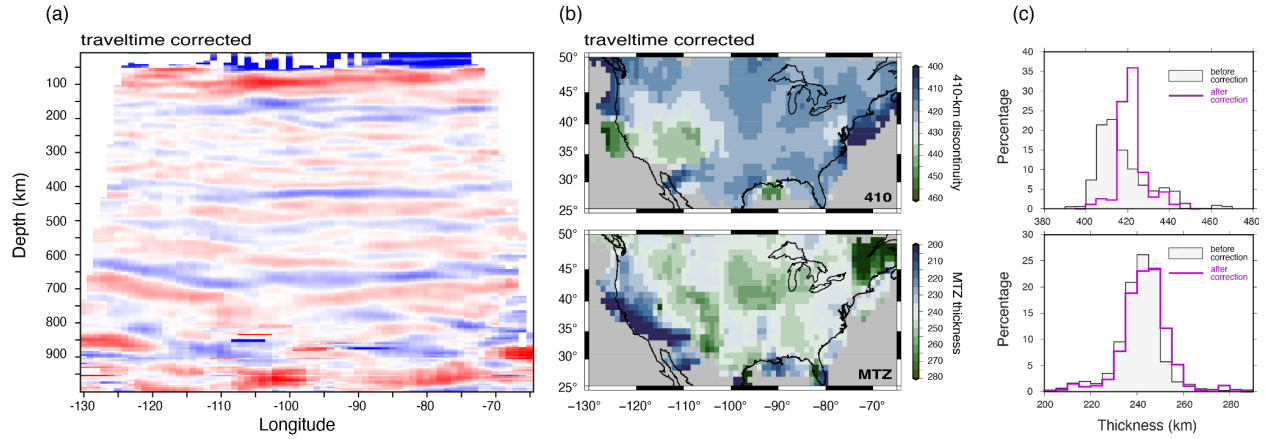


Figure 6. Depth of the 410 (in a) and the thickness of the transition zone (in b) estimated after ray-theoretical travel time corrections have been applied. Panels c and d show histograms of the resolved 410 depth and the thickness of the MTZ beneath the USArray with (black line) and without (purple line) travel time corrections. Compare with Figure 4b.

4. Resolution tests using spectral-element-method waveforms

We analyze synthetic waveforms to test the robustness of our CRP imaging approach, the resolution of 410 and 660 undulations from long-period Ssds waveform data, and the accuracy of ray-theoretical corrections. The waveforms are computed using SPECFEM3D-Globe software (e.g., Komatitsch and Tromp, 2002; Komatitsch et al., 2016) modified by us to allow for undulations of the 410 and 660. The seven test structures are PREM, S40RTS (Figure 7a), SEMUCB-WM1, TX2015, and structures T2, T5 and T8 (Figure 7b). In each structure, the density and velocities in the uppermost mantle extend to the surface. We remove the crust from seismic models to suppress reverberations in the crust that complicate the waveforms following the S wave.

The one-dimensional PREM structure with discontinuities at 220 km, 400 km, 670 km depth serves as a baseline test for determining artefacts in the CRP images unrelated to 3-D structure in the upper mantle. In our calculations, S40RTS, SEMUCB-WM1, and TX2015 represent models of the 3-D shear velocity structure in the mantle. We do not include the crustal structure, adopt PREM as the reference structure for each of the three models, and assume the Voigt average shear-velocity variations in the anisotropic SEMUCB-WM1 model. The 220, 410 and 660 are horizontal boundaries at the same depths as in the PREM model. Models T2, T5, and T8 have the same layered velocity structure as PREM but the 410 and the 660 are sinusoidal boundaries with amplitudes of 15 km and wavelengths of 2°, 5°, and 8°, respectively. The undulations of the 410 and 660 are in the opposite sense so the thickness of the mantle transition zone between the 410 and the 660 varies up to 30 km with respect to the average of 270 km.

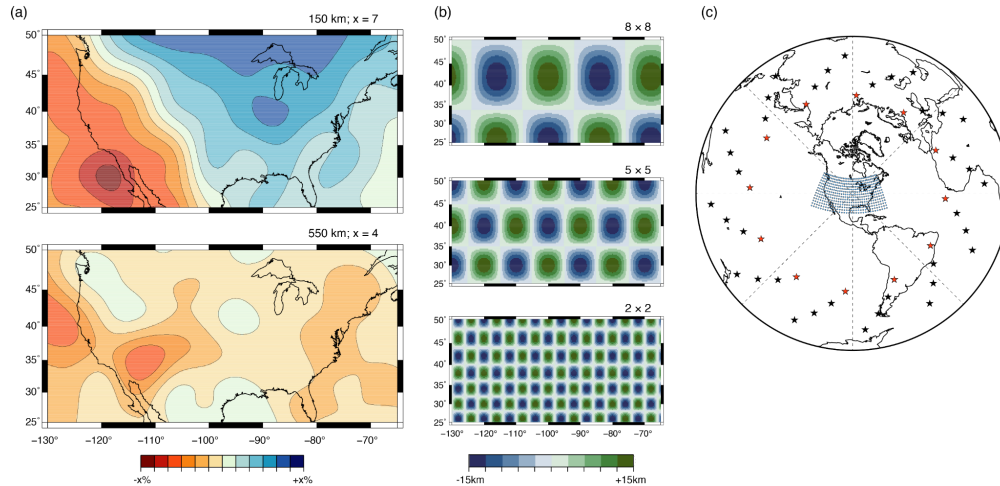


Figure 7. (a) Maps of the shear-velocity variation at (top) 150 km and (bottom) 500 km depth according to S40RTS. The east-west contrast across the US is similar for SEMUCB-WM1 and TX2015. (b) Harmonic undulations of the 410 and 660 for (from top to bottom) models T8, T5, and T2 with spatial wavelengths of 8°, 5°, and 2°. (c) Distribution of hypothetical earthquakes (stars) and stations (circles). For models PREM, S40RTS, T8 and T5 we compute waveforms for the twelve earthquakes indicated by red stars. For T2, we compute waveforms for these earthquakes and the additional 36 earthquakes indicated by black stars.

For each of the seven structures, we compute waveforms at periods longer than 10 s for 462 stations in a rectangular $2^\circ \times 2^\circ$ grid between longitudes 130° – 65° W and latitudes 25° – 50° N (Figure 7c). We calculate waveforms for 12 earthquakes uniformly distributed at a distance of 75° from $[-100^\circ\text{E}, 40^\circ\text{N}]$. We use 48 earthquakes distributed in a spiral for structure T2. The uniform data coverage is sufficient to investigate the effects of velocity heterogeneity on Ssds-S traveltimes and the resolution of 410 and 660 undulations using long-period Ssds reflections. Because of the high computational cost, we cannot afford to reproduce the source-station combinations in the data and, therefore, we cannot estimate CRP mapping artefacts due to inhomogeneous slowness and azimuthal sampling.

4.1 Testing ray-theoretical traveltime corrections

Figure 8 shows the CRP images along the 35° N parallel in the central region of the model domain determined for the PREM and S40RTS models. Supplementary Figure 2 shows similar CRP images for SEMUCB-WM1 and TX2015. The CRP image for PREM in Figure 8a is the ideal case as the assumed velocity structure of the mantle is identical to the structure used to calculate traveltimes and ray paths. Artifacts are entirely due to the implementation of the CRP mapping procedure, the limited frequency band of the waveforms, and wave interference. PREM's velocity discontinuities at 220, 400, and 670 km depth are resolved about 10 km shallower in the mantle because the crust is not included in the waveform computations. Since the waveforms are computed for periods longer than 10 s and since shear wave speed increases with depth, reflectors at larger depths are more stretched than at shallower depths. The imaged 660 is therefore about 60% stronger than the 410 even though the impedance contrast at the 660 is a factor of two stronger than at the 410. Overall, the CRP image derived from PREM waveforms is free of artificial layering between 150 km and 750 km depth. The side lobes of the 660 near -65° E are artifacts near the boundaries of the station grid. Layering near 100 km depth, which is especially strong near the center of the CRP image, shows that the Ssds reverberation is not an ideal wave type for imaging the uppermost

mantle when the analysis is based on shallow earthquakes. The arch-shaped structure below 750 km depth is likely the projection of shallow SS precursors misinterpreted as Ssds reflections deep in the transition zone as discussed in section 2.1.

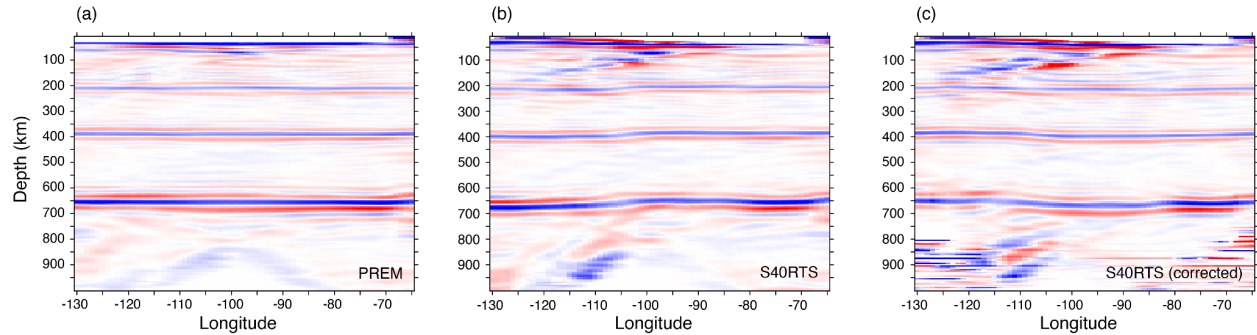


Figure 8. CRP image along the 35° parallel determined for (a) PREM synthetics, (b) S40RTS synthetics, and (c) S40RTS synthetics after ray-theoretical corrections have been applied.

The CRP image derived from S40RTS waveforms is more complex (**Figure 8b**). The 410 and 660 deepen from east to west because S40RTS predicts that Ssds travel times through the upper mantle are shorter beneath the central and eastern US than beneath the western US and we use the PREM velocity structure to convert traveltimes to reflector depths. The velocity heterogeneity in S40RTS causes misalignments of Ssds signals and therefore fluctuations in the strength of 410 and 660 from west to east by up to a factor of two. For example, the 660 appears as a relatively weak reflecting boundary between longitudes -120°E and -110°E, near the transition between the low-velocity upper mantle of the western US and the high-velocity upper mantle beneath the central US. In addition, spurious reflectors are particularly strong between -120°E and -100°E, where horizontal gradients in the uppermost mantle are strongest. It is difficult to identify how complex wave propagation produced the complexity in the CRP image but we note that the CRP image based on USArray waveforms is also most complex for the western US and a tilted reflective structure in the upper mantle has been observed by SB19 in their data image, albeit with an eastward dip and a greater depth extent.

Figure 8c shows the CRP image based on the S40RTS synthetics after applying ray-theoretical traveltime corrections following the procedure outlined in section 4.3. The traveltime corrections do not remove, and may even amplify the CRP image artifacts for depths shallower than 100 km and deeper than 750 km. More significantly, the ray-theoretical calculations appear to overpredict the contribution of shear-velocity heterogeneity to the Ss410s-S and Ss660s-S difference times. After traveltime correction, the 410 and 660 are projected shallower beneath the western US than the central US, opposite to the imaged depths of the 410 and 660 prior to corrections.

The inaccuracy of ray theory in predicting the shear-wave traveltime perturbations is illustrated further in **Figure 9**. It shows the estimated depths of the 410 and the 660 and the thickness of the MTZ based on the 1-D CRP method applied to synthetic waveforms computed for S40RTS. **Supplementary Figure 3** shows that we obtain similar results for SEMUCB-WM1 and TX2015. The total variation in the depths of the 410 and 660 is about 15–20 km. As expected, the depth of the 410 (**Figure 9a**) mimics the shear-velocity variations in the upper mantle of S40RTS (**Figure 7a**) and the S-wave traveltime delay map shown in **Figure 5**. The depth variation of the 660 (**Figure 9b**) is slightly different because shear velocity variations in the

MTZ also influence the traveltimes of Ss660s. Variations in the thickness of the MTZ (Figure 9c) of about 10 km are small compared to the depth variations of the 410 and 660 because shear velocity variations in the MTZ are much weaker than in the uppermost mantle.

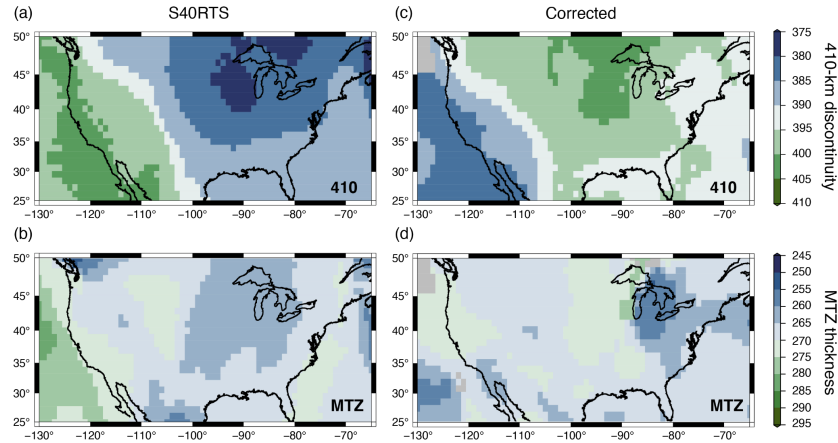


Figure 9. Depths of the 410 (top row) and the thickness of the transition zone (bottom row). Panels (a) and (b) are estimated from spectral-element-method seismograms calculated for model S40RTS. Panels (c) and (d) show the same estimates after ray-theoretical time shifts have been applied to the waveforms.

If ray-theoretical traveltime corrections are precise, we must expect that the CRP images of the ray-theoretical corrected S40RTS, SEMUCB-WM1 and TX2015 waveforms are similar to the CRP image for the PREM model because the 410 and 660 are horizontal boundaries in all models. However, we find this not to be the case. While the elevation of the 410 and 660 beneath the western US (by 10 and 11 km, respectively) and their depressions beneath the central-eastern US (by 11 and 12 km, respectively) have the expected trends, the corrections are larger than expected ray-theoretically. In the corrected image, the 410 and 660 are shallower in the western US than in the eastern US (Figure 9d and 9e) opposite to the uncorrected CRP image (Figure 9g and 9h). The corrections are least accurate for the central-eastern US. Here, the depth correction of the 410 is 10 km but expected to be 5 km. In the western US the inferred and predicted depth correction differ by a factor of 1.7.

4.2 The resolution of 410 and 660 undulations

Figure 10 shows the depths of the 410 and the 660 and the thickness of the MTZ resolved for models T2, T5, and T8. The checkerboard pattern of the undulations on the 410 and 660 are resolved for T5 and T8 but the amplitude of the undulations is underestimated. The resolved thickness of the MTZ varies, on average, 12 km and 6 km less than in the original T8 and T5 models. The resolution of the undulations in T2 is poor despite using a larger set of waveforms for 48 earthquakes. From experiments we have found that the resolution does not improve if we densify the grid of stations to a 1-degree spacing (not shown in Figure 10). Therefore, fluctuations of the depth of the 410 or 660 with a wavelength of about 200 km are intrinsically unresolvable from long-period Ssds waveforms because the Fresnel zone of Ss410s and Ss660s in the upper mantle at the dominant frequency of about 0.05 Hz are about 500 km, much wider than the undulations of the 410 and 660 in T2.

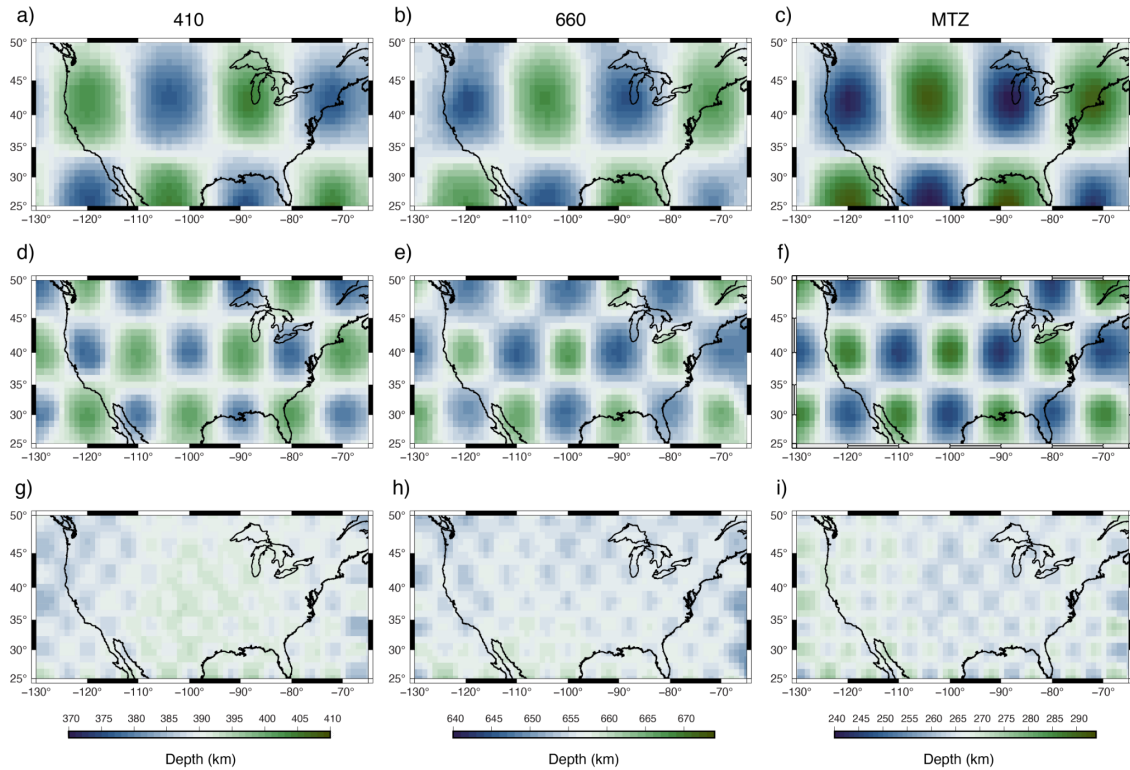


Figure 10. Depth maps of 410, 660, and MTZ thickness using the depth stack method for 8×8 (a, b, c), 5×5 (d, e, f), and 2×2 (g, h, i) input topography models.

5. Discussion and conclusions

The receiver-side S wave reverberation, denoted as Ssds, is a useful data type to map the shear velocity structure in the upper mantle, including undulations of the 410 and 660 mineral phase transitions. Ssds complement SS precursor and P-to-S wave conversion (i.e., receiver function) imaging of the mantle because of its unique wave path geometry. In agreement with the analysis by SB19, we observe in record sections of waveform stacks that the Ss410s-S and Ss660s traveltime differences vary by up to 10 s across stations from the USArray. If the traveltime differences are attributed entirely to 410 and 660 undulations, it implies that the 410 and 660 are 40–50 km deeper beneath the western US than the central and eastern US. In turn, this would mean that the geological contrast between the tectonically active western US and the stable central and eastern US persists as a temperature or compositional contrast in the mantle transition zone and thus a link between uppermost mantle and mantle transition zone dynamics.

However, the correlation between the resolved depth of the 410 (and the 660) and tomographic maps of the shear-velocity structure in the upper mantle is high. This indicates that velocity heterogeneity in the uppermost mantle contributes significantly to the Ss410s-S and Ss660s-S traveltimes and the spatial variations of the 410 depth inferred from common-reflection-point (CRP) imaging. Ray-theoretical corrections of traveltimes for velocity heterogeneity by shifting segments of the waveforms containing Ss410s and Ss660s prior to CRP stacking reduces the variation in the 410 depth by a factor of two.

For at least two reasons we find ray-theoretical corrections imprecise. First, seismic tomography has uncertainty. Global models S40RTS, SEMUCB-WM1, and TX2015 agree on the east–west contrast but disagree on the magnitude of the traveltime perturbations (see [Figure 4](#)). Each model underestimates the S-wave traveltime delay at USArray stations (see [Figure 5](#)) which is consistent with the fact that tomographic models underestimate the magnitude of traveltime and waveform perturbations. Hence, the effect on the estimated depths of the 410 and 660 depends on the chosen tomographic model. SB19 note that the traveltime corrections may introduce incoherence in the CRP images and use that as a factor in determining the value of traveltime corrections.

Second, our experiments with spectral-element method synthetics demonstrate that ray-theoretical predictions of the Ss410s-S and Ss660s traveltime differences are inaccurate. CRP images derived from waveforms computed for a mantle with 3-D velocity heterogeneity and horizontal phase boundaries show the expected deepening of the 410 and 660 below the western US and shallowing beneath the central and eastern US where the shear velocities are relatively low and high, respectively. After applying traveltime corrections for the 3-D wave speed structure, the 410 and 660 remain undulating boundaries. In fact, the 410 and the 660 in the corrected CRP image are deeper beneath the central-eastern US than beneath the western US, opposite to the uncorrected CRP image. This indicates that ray theory overpredicts the Ssds-S difference time by about a factor of two. This is the case for S40RTS, SEMUCB-WM1 and TX2015 and presumably also finer-scale regional tomographic models when finite-frequency effects are stronger. The inaccuracy of ray-theoretical predictions of the traveltime perturbations of long-period waves has been studied previously. For example, [Neele et al. \(1997\)](#) and [Zhao and Chevrot \(2003\)](#) have pointed out that the broad SS sensitivity kernels at the reflection points on the surface or the mantle discontinuities. [Bai et al. \(2011\)](#) and [Koroni and Trampert \(2013\)](#) illustrate how the finite wave effects affect CRP images built from SS precursors similarly to the study here.

Finally, we note that the resolution of the depths of the 410 and 660 depends on spatial scales of the undulations. Our experiments with spectral element method synthetics indicate that the Ssds-S traveltime difference is sensitive to $5^\circ \times 5^\circ$ and $8^\circ \times 8^\circ$ sinusoidal variations of the 410 and 660 depths albeit that the height of the undulations is underestimated. Spatial variations of the 410 and 660 on a $2^\circ \times 2^\circ$ scale are not resolvable because such variations are smaller than the width of the Fresnel zone of Ssds at a period of 10 s.

Although it is beyond the scope of this work, it is better to simultaneously estimate 410 and 660 topography and shear velocity heterogeneity in the mantle of multiple data sets (e.g., [Gu et al., 2003](#), [Moulik and Ekström, 2014](#)) using finite-frequency kernels that relate waveform perturbations to velocity heterogeneity and phase boundary topography (e.g., [Guo and Zhou, 2020](#)) or, preferably, using an adjoint tomography approach ([Koroni and Trampert, 2021](#)). Based on our experiments, the evidence for large-scale variations of the depth of the 410 beneath the USArray is weak. As is well established, estimates of the thickness of the MTZ are not affected strongly by shear velocity heterogeneity. We find the thickness of the MTZ to vary by about 10 km, which is consistent with the receiver-function study of USArray data by [Gao & Liu \(2014\)](#) and much smaller than global variations of the MTZ observed in SS precursors studies (e.g., [Flanagan & Shearer, 1998](#); [Chambers et al., 2005](#)).

Acknowledgments

This research was supported by the NSF (EAR-1644829). The facilities of IRIS Data Services, and specifically the IRIS Data Management Center, were used for access to waveforms, related metadata, and/or derived products used in this study. IRIS Data Services are funded through the Seismological Facilities for the Advancement of Geoscience (SAGE) Award of the National Science Foundation under Cooperative Support Agreement EAR-1851048. Data from the TA network were made freely available as part of the EarthScope USArray facility, operated by Incorporated Research Institutions for Seismology (IRIS) and supported by the National Science Foundation, under Cooperative Agreements EAR-1261681. The SPECMFEM3D_Globe software was downloaded from the Computational Infrastructure for Geodynamics (<https://geodynamics.org/>).

References

- Abt, D. L., Fischer, K. M., French, S. W., Ford, H. A., Yuan, H., & Romanowicz, B. (2010). North American lithospheric discontinuity structure imaged by Ps and Sp receiver functions. *Journal of Geophysical Research: Solid Earth*, 115(B9).
- Bai, L., Zhang, Y., & Ritsema, J. (2012). An analysis of SS precursors using spectral-element method seismograms. *Geophysical Journal International*, 188(1), 293-300.
- Bensen, G. D., Ritzwoller, M. H., & Shapiro, N. M. (2008). Broadband ambient noise surface wave tomography across the United States. *Journal of Geophysical Research: Solid Earth*, 113(B5).
- Bina, C. R., & Helffrich, G. (1994). Phase transition Clapeyron slopes and transition zone seismic discontinuity topography. *Journal of Geophysical Research: Solid Earth*, 99(B8), 15853-15860.
- Bowden, D. C., & Tsai, V. C. (2017). Earthquake ground motion amplification for surface waves. *Geophysical Research Letters*, 44(1), 121-127.
- Chambers, K., Woodhouse, J. H., & Deuss, A. (2005). Topography of the 410-km discontinuity from PP and SS precursors. *Earth and Planetary Science Letters*, 235(3-4), 610-622.
- Christensen, U. (1995). Effects of phase transitions on mantle convection. *Annual Review of Earth and Planetary Sciences*, 23(1), 65-87.
- Crotwell, H. P., Owens, T. J., & Ritsema, J. (1999). The TauP Toolkit: Flexible seismic travel-time and ray-path utilities. *Seismological Research Letters*, 70(2), 154-160.
- Courtier, A. M., Jackson, M. G., Lawrence, J. F., Wang, Z., Lee, C. T. A., Halama, R., ... & Chen, W. P. (2007). Correlation of seismic and petrologic thermometers suggests deep thermal anomalies beneath hotspots. *Earth and Planetary Science Letters*, 264(1-2), 308-316.
- Deng, K., & Zhou, Y. (2015). Wave diffraction and resolution of mantle transition zone discontinuities in receiver function imaging. *Geophysical Journal International*, 201(3), 2008-2025.
- Deuss, A., Redfern, S. A., Chambers, K., & Woodhouse, J. H. (2006). The nature of the 660-kilometer discontinuity in Earth's mantle from global seismic observations of PP precursors. *Science*, 311(5758), 198-201.
- Dziewonski, A. M., & Anderson, D. L. (1981). Preliminary reference Earth model. *Physics of the earth and planetary interiors*, 25(4), 297-356.
- Eddy, C. L., & Ekström, G. (2014). Local amplification of Rayleigh waves in the continental United States observed on the USArray. *Earth and Planetary Science Letters*, 402, 50-57.

- 525 Flanagan, M. P., & Shearer, P. M. (1998). Global mapping of topography on transition zone velocity discontinuities
526 by stacking SS precursors. *Journal of Geophysical Research: Solid Earth*, 103(B2), 2673-2692.
- 527 French, S. W., & Romanowicz, B. A. (2014). Whole-mantle radially anisotropic shear velocity structure from spectral-
528 element waveform tomography. *Geophysical Journal International*, 199(3), 1303-1327.
- 529 Gao, S. S., & Liu, K. H. (2014). Mantle transition zone discontinuities beneath the contiguous United States. *Journal*
530 *of Geophysical Research: Solid Earth*, 119(8), 6452-6468.
- 531 Grand, S. P., & Helmberger, D. V. (1984). Upper mantle shear structure of North America. *Geophysical Journal*
532 *International*, 76(2), 399-438.
- 533 Guo, Z., & Zhou, Y. (2020). Finite-frequency imaging of the global 410-and 660-km discontinuities using SS
534 precursors. *Geophysical Journal International*, 220(3), 1978-1994.
- 535 Haugland, S. M., Ritsema, J., Sun, D., Trampert, J., & Koroni, M. (2020). Common reflection point mapping of the
536 mantle transition zone using recorded and 3-D synthetic ScS reverberations. *Geophysical Journal International*,
537 220(1), 724-736. Hopper, E., & Fischer, K. M. (2018). The changing face of the lithosphere-asthenosphere
538 boundary: Imaging continental scale patterns in upper mantle structure across the contiguous US with Sp
539 converted waves. *Geochemistry, Geophysics, Geosystems*, 19(8), 2593-2614.
- 540 Komatitsch, D., & Tromp, J. (2002). Spectral-element simulations of global seismic wave propagation—I. Validation.
541 *Geophysical Journal International*, 149(2), 390-412.
- 542 Komatitsch, D., Xie, Z., Bozdağ, E., Sales de Andrade, E., Peter, D., Liu, Q., & Tromp, J. (2016). Anelastic sensitivity
543 kernels with parsimonious storage for adjoint tomography and full waveform inversion. *Geophysical Journal*
544 *International*, 206(3), 1467-1478.
- 545 Koroni, M., & Trampert, J. (2016). The effect of topography of upper-mantle discontinuities on SS precursors.
546 *Geophysical Journal International*, 204(1), 667-681.
- 547 Laske, G., Masters, G., Ma, Z., & Pasyanos, M. (2013, April). Update on CRUST1. 0—A 1-degree global model of
548 Earth's crust. In *Geophys. res. abstr* (Vol. 15, p. 2658).
- 549 Li, X., Yuan, X., & Kind, R. (2007). The lithosphere-asthenosphere boundary beneath the western United States.
550 *Geophysical Journal International*, 170(2), 700-710.
- 551 Liu, T., & Shearer, P. M. (2021). Complicated Lithospheric Structure Beneath the Contiguous US Revealed by
552 Teleseismic S-Reflections. *Journal of Geophysical Research: Solid Earth*, 126(5), e2020JB021624.
- 553 Lu, C., & Grand, S. P. (2016). The effect of subducting slabs in global shear wave tomography. *Geophysical Journal*
554 *International*, 205(2), 1074-1085.
- 555 Mancinelli, N. J., Fischer, K. M., & Dalton, C. A. (2017). How sharp is the cratonic lithosphere-asthenosphere
556 transition?. *Geophysical Research Letters*, 44(20), 10-189.
- 557 Neele, F., de Regt, H., & Van Decar, J. (1997). Gross errors in upper-mantle discontinuity topography from underside
558 reflection data. *Geophysical Journal International*, 129(1), 194-204.
- 559 Park, S., Tsai, V. C., & Ishii, M. (2019). Frequency-dependent P wave polarization and its subwavelength near-surface
560 depth sensitivity. *Geophysical Research Letters*, 46(24), 14377-14384.
- 561 Ritsema, J., Deuss, A. A., Van Heijst, H. J., & Woodhouse, J. H. (2011). S40RTS: a degree-40 shear-velocity model
562 for the mantle from new Rayleigh wave dispersion, teleseismic traveltime and normal-mode splitting function
563 measurements. *Geophysical Journal International*, 184(3), 1223-1236.
- 564 Rychert, C. A., Rondenay, S., & Fischer, K. M. (2007). P-to-S and S-to-P imaging of a sharp lithosphere-
565 asthenosphere boundary beneath eastern North America. *Journal of Geophysical Research: Solid Earth*, 112(B8).

566 Shearer, P. M. (1990). Seismic imaging of upper-mantle structure with new evidence for a 520-km discontinuity.
567 *Nature*, 344(6262), 121-126.

568 Shearer, P.M., Constraints on upper-mantle discontinuities from observations of long-period reflected and converted
569 phases, *J. Geophys. Res.*, 96, 18,147-18,182, 1991.

570 Shearer, P. M., & Buehler, J. (2019). Imaging upper-mantle structure under USArray using long-period reflection
571 seismology. *Journal of Geophysical Research: Solid Earth*, 124(9), 9638-9652.

572 Revenaugh, J., & Jordan, T. H. (1991). Mantle layering from ScS reverberations: 2. The transition zone. *Journal of*
573 *Geophysical Research: Solid Earth*, 96(B12), 19763-19780.

574 Schmandt, B., & Lin, F. C. (2014). P and S wave tomography of the mantle beneath the United States. *Geophysical*
575 *Research Letters*, 41(18), 6342-6349.

576 Stixrude, L., & Lithgow-Bertelloni, C. (2011). Thermodynamics of mantle minerals-II. Phase equilibria. *Geophysical*
577 *Journal International*, 184(3), 1180-1213.

578 Tromp, J., Tape, C., & Liu, Q. (2005). Seismic tomography, adjoint methods, time reversal and banana-doughnut
579 kernels. *Geophysical Journal International*, 160(1), 195-216.

580 Van der Lee, S., & Nolet, G. (1997). Upper mantle S velocity structure of North America. *Journal of Geophysical*
581 *Research: Solid Earth*, 102(B10), 22815-22838.

582 Waszek, L., Tauzin, B., Schmerr, N. C., Ballmer, M. D., & Afonso, J. C. (2021). A poorly mixed mantle transition
583 zone and its thermal state inferred from seismic waves. *Nature Geoscience*, 1-7.

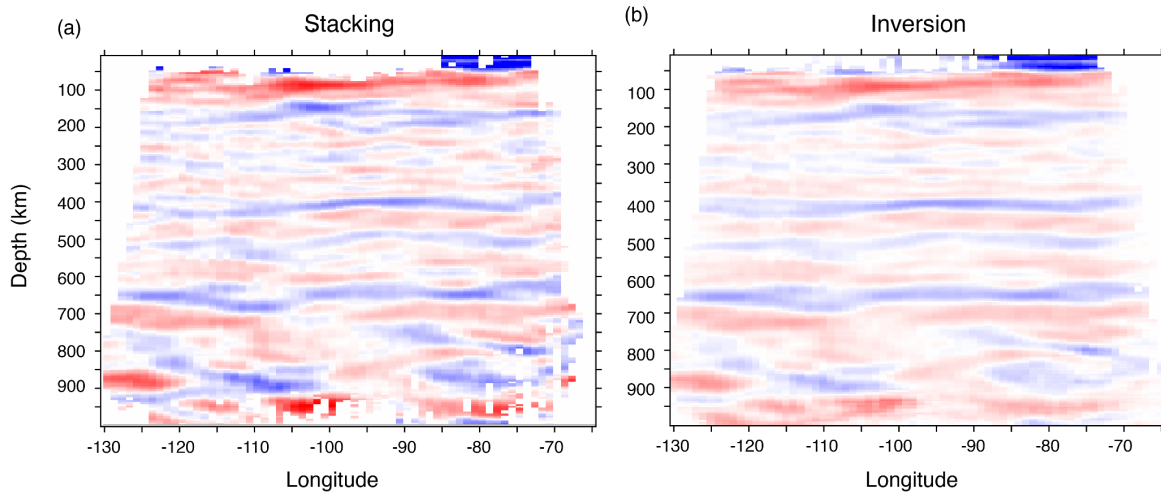
584 Xu, W., Lithgow-Bertelloni, C., Stixrude, L., & Ritsema, J. (2008) The effect of bulk composition on seismic structure,
585 *Earth and Planetary Science Letters*, 275, 70-79, doi:10.1016/j.epsl.2008.08.012.

586 Yuan, H., & Romanowicz, B. (2010). Lithospheric layering in the North American craton. *Nature*, 466(7310), 1063-
587 1068.

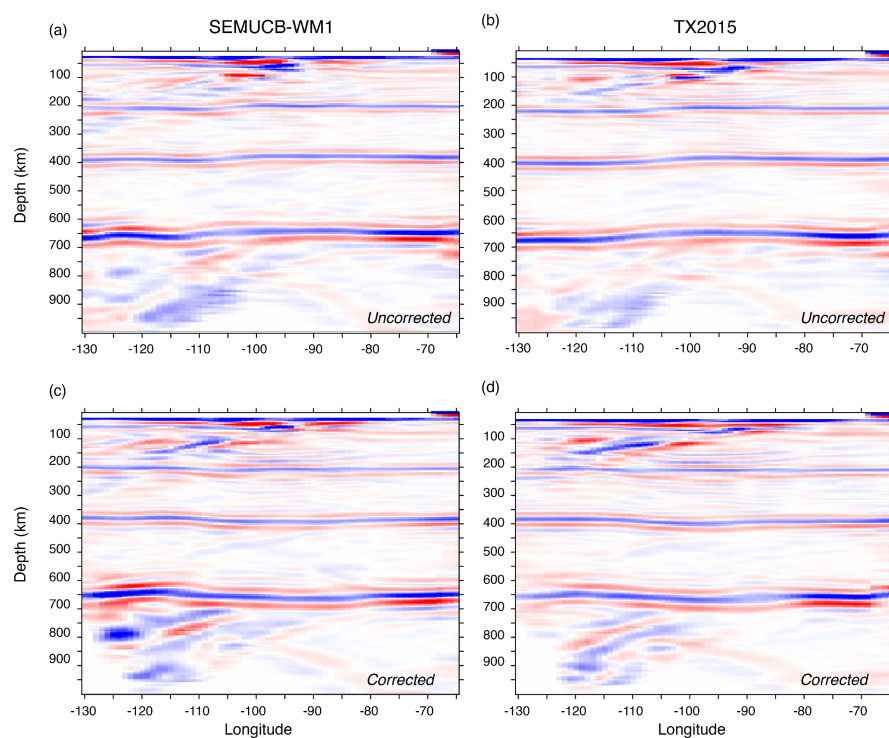
588 Zhao, L., & Chevrot, S. (2003). SS-wave sensitivity to upper mantle structure: Implications for the mapping of
589 transition zone discontinuity topographies. *Geophysical research letters*, 30(11).

590

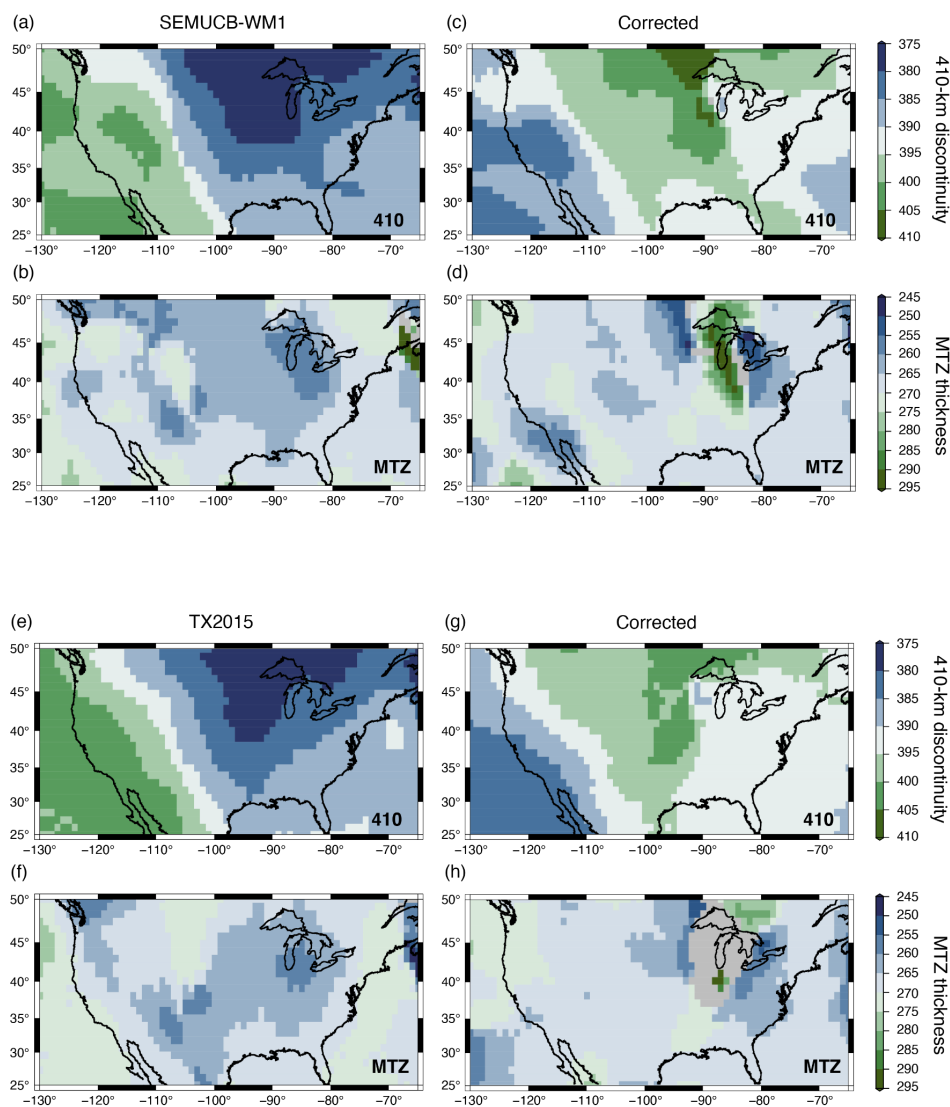
591



Supplementary Figure 1. Vertical section of the CRP image along 40°N determined by our stacking method (a) and SB19's inversion method (b). See also Figure 4. Because the CRP imaging is based on 1-D wave propagation, it is difficult to estimate the amplitude of Ssds produced by local reflecting boundaries and undulating global discontinuities. If a reflecting boundary exists only beneath the source, the source-side contribution to Ssds is underestimated because half of the amplitude of Ssds is attributed to a reflection on the receiver side. On the other hand, the source-side reflection is overestimated if a reflection boundary exists only beneath the USArray. We expect therefore that the impedance contrasts of reflecting boundaries are uncertain despite our large set of amplitudes from earthquakes at all azimuths from the USArray. Our implementation of the inversion approach results in a misfit reduction smaller than 10%, underscoring the difficulty to separate source-side and receiver-side contributions to Ssds waveforms and that the impedance contrasts are uncertain. The synthetic tests by SB19 also illustrate this.



Supplementary Figure 2. CRP image along the 35° parallel determined for (a and c) SEMUCB-WM1 and (b and d) TX2015 synthetics without (in a and b) and with (in c and d) ray-theoretical corrections.



Supplementary Figure 3. Depths of the 410 and the thickness of the MTZ obtained by CRP imaging spectral-element-method seismograms computed for model SEMUCB-WM1 (a–d) and TX2015 (e–h) with and without ray-theoretical traveltimes corrections. Compare to Figure 9.